Advanced Fiber Materials (2022) 4:520–531
https://doi.org/10.1007/s42765-021-00125-4

RESEARCH ARTICLE

Hybrid Polymer Membrane Functionalized PBO Fibers/Cyanate Esters Wave-Transparent Laminated Composites

Zheng Liu[1] · Xiaoli Fan[2] · Lei Cheng[3] · Junliang Zhang[1] · Lin Tang[1] · Yusheng Tang[1] · Jie Kong[1] · Junwei Gu[1]

Received: 21 October 2021 / Accepted: 5 December 2021 / Published online: 10 January 2022

Abstract

Hybrid polymer membrane (TA-APTES), synthesized by tannic acid (TA) and aminopropyl trethoxysilane (APTES) based on the Schiff's base and Michael addition reaction, is deposited on the surface of poly(*p*-phenylene-2, 6-benzobisoxazole) (PBO) fibers, and then grafted with epoxy-terminated polysesquisiloxane (POSS) to obtain POSS-*g*-PBO@TA-APTES fibers. The POSS-*g*-PBO@TA-APTES fibers reinforced bisphenol A dicyanate ester (BADCy) resins (POSS-*g*-PBO@TA-APTES fibers/BADCy) wave-transparent laminated composites are prepared. The interlaminar shear strength and flexural strength of POSS-*g*-PBO@TA-APTES fibers/BADCy composites are respectively enhanced from 36.7 and 587.4 MPa to 42.8 and 645.8 MPa, increased by 16.6% and 9.9% compared with those of PBO fibers/BADCy composites. At 1 MHz, the corresponding dielectric constant and dielectric loss are reduced to 2.85 and 0.0047, respectively, lower than those of PBO fibers/BADCy (3.06 and 0.006) composites. Meanwhile, the simulated wave transmittance rate of POSS-*g*-PBO@TA-APTES fibers/BADCy composites with the thicknesses of 1.5–3.5 mm is higher than 86.2% at 0.3–40 GHz. The volume resistivity and breakdown strength of POSS-*g*-PBO@TA-APTES fibers/BADCy composites are 2.8×10^{15} Ω·cm and 19.80 kV/mm, higher than PBO fibers/BADCy composites (2.2×10^{15} Ω·cm and 17.69 kV/mm), respectively. And the corresponding heat resistant index is 221.5 °C, lower than PBO fibers/BADCy composites (229.6 °C).

Keywords Poly(*p*-phenylene-2, 6-benzobisoxazole) fibers · Bisphenol A dicyanate ester resins · Wave-transparent laminated composites · Interlaminar shear strength · Surface functionalization

✉ Junliang Zhang
junliang.zhang@nwpu.edu.cn

✉ Junwei Gu
gjw@nwpu.edu.cn; nwpugjw@163.com

[1] Shaanxi Key Laboratory of Macromolecular Science and Technology, School of Chemistry and Chemical Engineering, Northwestern Polytechnical University, Xi'an, Shaanxi 710072, People's Republic of China

[2] State Key Laboratory of Solidification Processing, Northwestern Polytechnical University, Xi'an, Shaanxi 710072, People's Republic of China

[3] Aerospace Research Institute of Materials and Processing Technology, Beijing 100076, People's Republic of China

Introduction

Polymer matrix wave-transparent composites can effectively protect the electromagnetic equipments inside antenna system from adverse external environment and ensure high electromagnetic wave transmission, which are widely used as electromagnetic window materials for military weapons and civilian telecommunication base stations [1, 2]. However, with the rapid development of the new generation of military equipment and 5G telecommunication, higher requirements of mechanical properties and wave-transparent performances are put forward for advanced polymer matrix wave-transparent composites [3].

Compared with quartz fibers [4, 5], basalt fibers [6], and aramide fibers [7, 8], the high modulus poly(*p*-phenylene-2, 6-benzobisoxazole) (PBO) fibers possess superior mechanical properties, better chemical and thermal stability, and ultra-lower dielectric constant (ε) and dielectric loss (tanδ) (Table S1) [9, 10]. However, the interfacial bonding strength of PBO fibers reinforced polymer matrix laminated composites is extremely weak [11, 12]. Besides, the poor interfacial compatibility between PBO fibers and polymer matrix will produce strong interfacial polarization under external electric field, which would lead to larger ε and tanδ values [13].

As far as we know, chemical etching [14], radiation treatment [15], plasma treatment [16], coating [3, 17], and grafting [18, 19], etc., are usual surface modification methods of PBO fibers. Chemical etching, radiation treatment, and plasma treatment methods apply strong acid or high-energy ray to etch PBO fibers, which can generate active groups to improve the surface chemical inertness of PBO fibers [20, 21]. However, strong acid and high-energy ray would destruct the structure of PBO fibers. Coating and/or grafting an active layer on the surface of PBO fibers can effectively improve the chemical inertia of PBO fibers without compromising the mechanical properties [22, 23]. Liu et al. coated the synthesized hydroxyphosphide castor oil (PCO) on PBO fibers followed by blending with epoxy resins (E-51). When the ratio of PCO to E-51 was 3:1, the single fiber pull-out strength of PBO fiber/PCO/epoxy resins composites was 12.03 MPa, increased by 154.8% [24]. Hu et al. prepared graphene-based coaxial hybrid PBO fibers (PBO-CHFs) by uniformly coating graphene and metal–organic framework hybrid layer on PBO fibers. The corresponding interlaminar shear strength (ILSS) of PBO-CHFs fibers/epoxy resins composites was 74.56 MPa, increased by 17.8% [25].

Dopamine (DA) can self-polymerize to form polydopamine (PDA) layers on the surface of various substrates by mimicking the adhesion mechanism of mussels. Chen et al. grafted graphene oxide onto the surface of PBO fibers coated by PDA, which significantly increased its roughness and UV resistance. The ILSS of the modified PBO fibers/epoxy resins composites was 68.2 MPa in compare with the PBO fibers/epoxy resins composites (40.4 MPa) [26]. Shao et al. coated PDA on PBO fibers, and then fixed BN nanosheets on the above PBO fibers to obtain BN-PDA-PBO fibers. Compared with PBO fibers/polyurethane (TPU), the ILSS of BN-PDA-PBO/TPU composites increased to 70.45 MPa [27]. In our pervious work, Gu et al. utilized PDA and KH-560 functionalized PBO (KH-560/PBO@PDA) fibers as reinforcement, and fluorinated bisphenol A cyanate (*m*-BADCy) resins as matrix to prepare KH-560/PBO@PDA fibers/*m*-BADCy laminated composites. The ILSS and flexural strength were respectively 49.5 and 652.2 MPa, better than those of the PBO fibers/*m*-BADCy composites (39.9 and 601.6 MPa). And the corresponding ε and tanδ values decreased to 2.86 and 0.00576, respectively [28].

Tannic acid (TA), a type of polyphenol extracted from plants, is similiar to DA, and can rapidly, gently, and stably adhere to the surface of various materials (polymers, metals and their oxides, inorganic non-metallic materials, etc.) through oxidative self-polymerization, which enables the simple and efficient surface functionalization of the substrates [29, 30]. Meanwhile, the tannic acid-aminopropyl trethoxysilane (TA-APTES) hybrid membrane, generated by the reaction of TA oxidation with 3-aminopropyl trethoxysilane (APTES), has a large number of reactive groups (hydroxyl and amino groups, etc.), which could provide abundant chemical reaction sites for secondary functionalization [31, 32], which is very attractive for surface functionalization of PBO fibers [33].

In this paper, the TA-APTES hybrid membrane, synthesized by TA and APTES via Schiff's base and Michael addition reaction, is constructed on the surface of PBO fibers by *in-situ co*-deposition method, and then grafted with polysesquisiloxane (POSS) to prepare POSS-*g*-PBO@TA-APTES fibers (Fig. 1). And the POSS-*g*-PBO@TA-APTES fibers are utilized as reinforcement, and bisphenol A dicyanate ester (BADCy) resins with excellent dielectric properties, outstanding mechanical properties and heat resistance [34–36] as matrix to prepare POSS-*g*-PBO@TA-APTES fibers reinforced BADCy resins (POSS-*g*-PBO@TA-APTES fibers/BADCy) wave-transparent laminated composites. Fourier transform infrared (FTIR) spectroscopy, X-ray photoelectron spectroscopy (XPS), scanning electron microscopy (SEM), and atomic force microscopy (AFM) are used to analyze the composition and morphologies of PBO fibers before and after surface functionalization. The effects of synergistic functionalization for POSS-*g*-PBO@TA-APTES fibers on the mechanical properties, wave-transparent performance, electrical insulation properties, and heat resistance of POSS-*g*-PBO@TA-APTES fibers/BADCy composites are investigated.

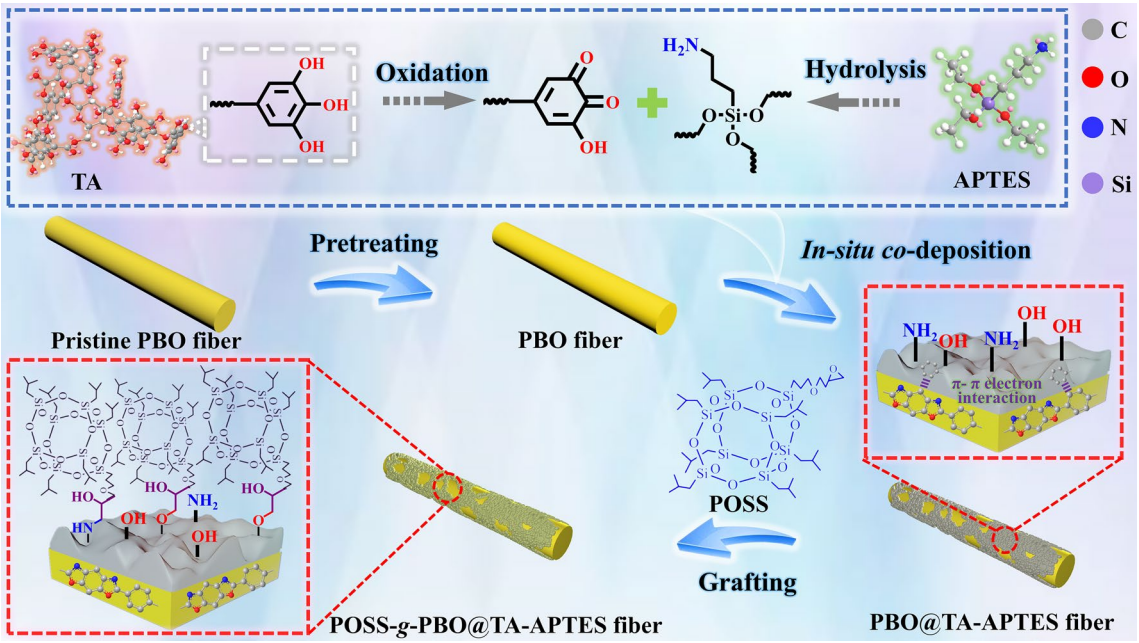

Fig. 1 Schematic diagram of preparation for POSS-*g*-PBO@TA-APTES fiber

Results and Discussion

PBO Fibers Before and After Surface Functionalization

Figure 2a shows the FTIR spectra of PBO fibers before and after surface functionalization. The absorption peaks at 3059, 1614, and 1556 cm^{-1} are attributed to the vibration of unsaturated C–H, C=C, and C–C on the benzene ring of PBO fibers, respectively. Moreover, peaks at 1630 and 1053 cm^{-1} correspond to the vibration of C=N and C–O–C in oxazole ring of PBO fibers, respectively. After surface functionalization, the wide absorption peak at 3500−3300 cm^{-1} in PBO@TA-APTES fibers can be attributed to the vibration of $–NH_2$, –NH–, and –OH in the TA-APTES hybrid membrane. In addition, the characteristic peaks of C=O and Si–O appear at 1705 and 1053 cm^{-1}, indicating that TA-APTES membrane is successfully deposited on the surface of PBO fibers. C–H stretching vibration peaks at 2916 and 2848 cm^{-1} can be attributed to the alkyl groups of POSS structure. Meanwhile, the absorption peak at 3417 cm^{-1} in POSS-*g*-PBO@TA-APTES fibers is attributed to the vibration of –NH– and –OH, which would be caused by the reaction of the epoxy group of POSS with $–NH_2$ and –OH of TA-APTES [37].

Figure 2b shows the TGA curves of PBO fibers before and after surface functionalization. Pristine PBO fibers show excellent heat resistance showing negligible weight loss before 650 °C. The weight loss rate of PBO@TA-APTES fibers gradually increases with the increase of temperature. Moreover, the weight loss rates of PBO@TA-APTES fibers are higher than that of pristine PBO fibers at the same temperature, which is caused by the decomposition of TA-APTES membrane. For POSS-*g*-PBO@TA-APTES fibers, the TGA curve shows a weight loss at 284.1 °C, mainly attributed to the thermal decomposition of POSS on the surface (Fig. S1). Diffraction peaks with 2θ degrees of 16.22° (200), 25.76° (010), 27.62° (210), and 32.70° (400) in the XRD spectra of Fig. 2c are corresponded to the main crystal planes of PBO fibers, indicating that the crystal structures of PBO fibers are not damaged after synergistic functionalization of TA-APTES membrane and POSS.

Figure 2d demonstrates the XPS spectra of PBO fibers before and after surface functionalization, and the concentration of corresponding elements can be seen in Fig. 2e. PBO@TA-APTES fibers show the peaks of Si 2 s and Si 2p and the content of O element significantly increases compared to pristine PBO fibers, which can be attributed to the large number of the phenolic hydroxyl groups in TA-APTES membrane. After grafting POSS, the Si and O element contents on the surface of PBO@TA-APTES fibers increase. Besides, PBO@TA-APTES fibers (Fig. 2d″) show peaks of $–NH_2$ and –NH– at 401.8 and 400.7 eV, respectively, indicating TA-APTES membrane is successfully deposited on PBO fibers. Moreover, the peak intensity of $-NH_2$ on the surface of POSS-*g*-PBO@TA-APTES fibers (Fig. 2d‴) is significantly reduced, which is due to the surface grafting reaction between $-NH_2$ and the epoxy group of POSS under acidic conditions Fig. 2f.

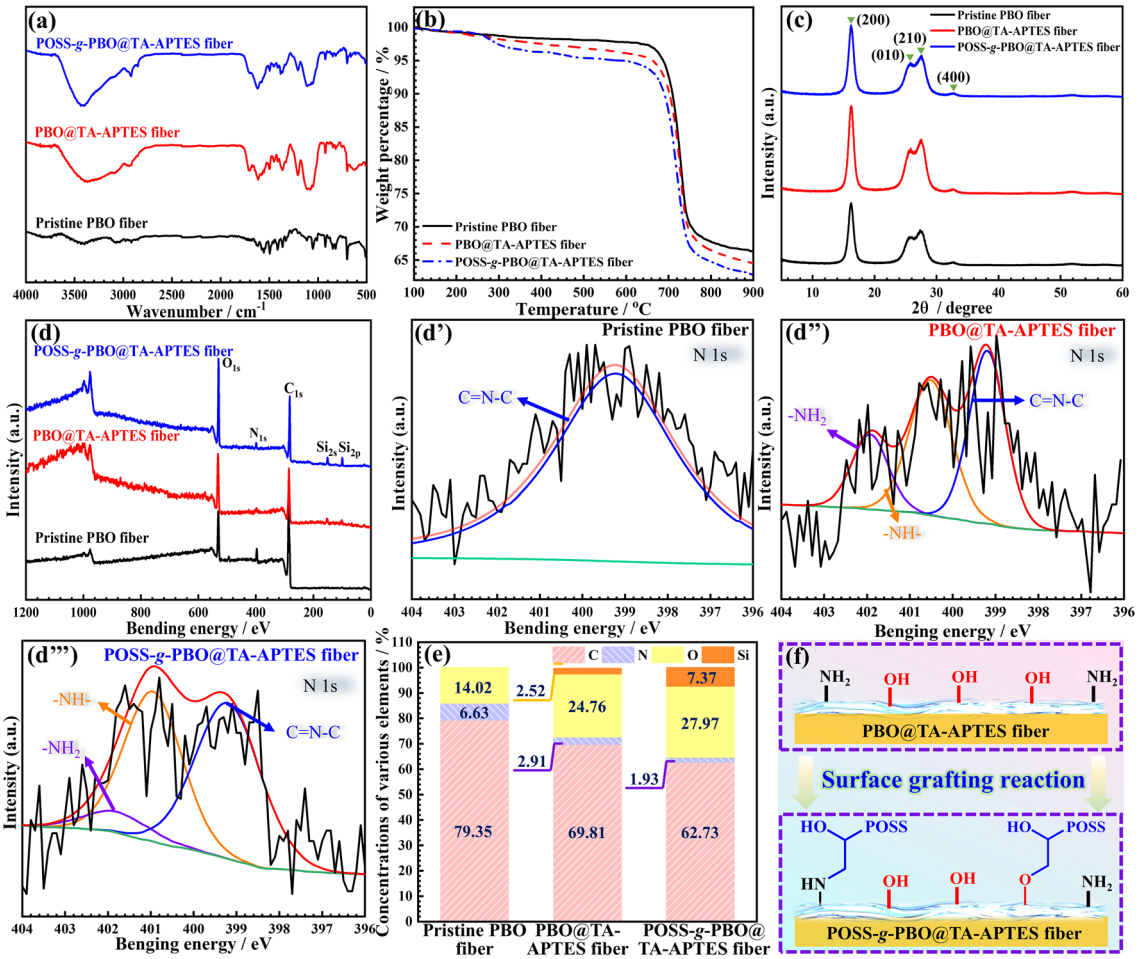

Fig. 2 FTIR (**a**), TGA (**b**), XRD (**c**), and XPS (**d**) curves of pristine PBO, PBO@TA-APTES, and POSS-*g*-PBO@TA-APTES fibers; Corresponding concentration of various elements (**e**); Schematic diagram of POSS grafting mechanism (**f**)

Figure 3 demonstrates the SEM (a–c) and AFM (d–f) morphologies of PBO fibers before and after surface functionalization. A uniform TA-APTES layer is observed on the PBO@TA-APTES fibers surface. The corresponding surface roughness increases from 15 nm of pristine PBO fibers (Fig. 3d) to 47 nm (Fig. 3e). This can be attributed to the hydrophilic nanospheres formed through TA oxidation and APTES hydrolysis products. Additionally, the surface of POSS-*g*-PBO@TA-APTES fibers displays increased amount of coating. The corresponding surface roughness is further increased to 52 nm (Fig. 3f). Besides, EDS spectra demonstrate that C, N, and Si elements are evenly distributed on the POSS-*g*-PBO@TA-APTES fibers (Fig. 3c′–c‴), suggesting the even distribution of TA-APTES and POSS hybrid membrane.

Figure 4a, b show the single fiber tensile strength and retention of pristine PBO, PBO@TA-APTES, and POSS-*g*-PBO@TA-APTES fibers under different UV aging time, respectively. PBO@TA-APTES (5.2 GPa) and POSS-*g*-PBO@TA-APTES (5.1 GPa) fibers display slightly decreased single fiber tensile strength in compare with pristine PBO fibers (5.4 Ga). Besides, the single fiber tensile strength and retention of pristine PBO, PBO@TA-APTES, and POSS-*g*-PBO@TA-APTES fibers decrease gradually with the increase of UV aging time due to the gradual destruction of oxazole rings of PBO fibers under UV irradiation [38]. After 288 h irradiation by UV lights, the absorption peaks of –OH, $–NH_2$, and –C=O– appear in the FTIR spectrum of pristine PBO (Fig. 4c). As shown by the SEM images of the surface for pristine PBO fiber in Fig. 4e1–3, the degradation products gradually increase with the increase of UV aging time (96–192 h). After 288 h irradiation by UV lights, there are a lot of obvious defects on the surface of pristine PBO fibers, which significantly reduces the single fiber tensile strength. Compared with the pristine PBO fibers (2.7 GPa and 50.0%), the single fiber tensile strength and retention rate of the PBO@TA-APTES fibers are 3.0 GPa and 57.7%, respectively, under the same UV aging time (288 h). This is because a large number of benzene rings existing in the uniform TA-APTES layer on the

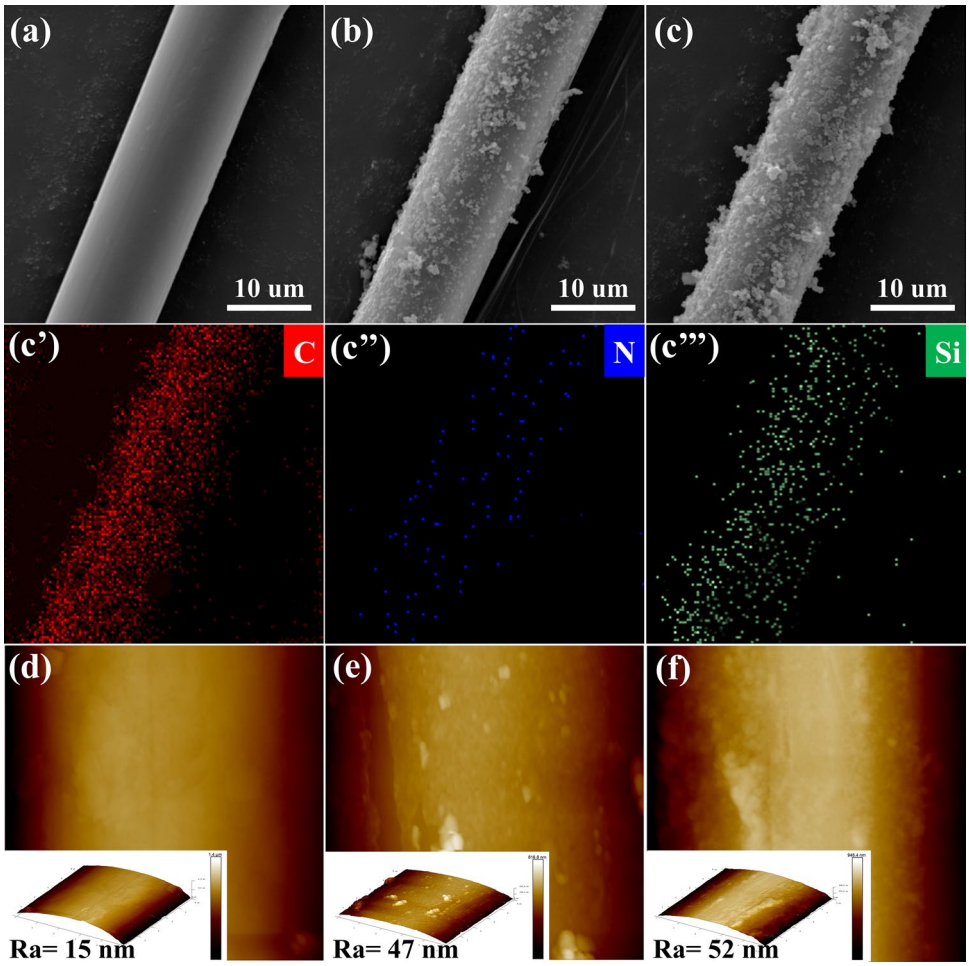

Fig. 3 SEM and AFM morphologies of the pristine PBO (**a**, **d**), PBO@TA-APTES (**b**, **e**), and POSS-*g*-PBO@TA-APTES fibers (**c**, **f**); EDS images of POSS-*g*-PBO@TA-APTES fibers (**c**′–**c**‴)

surface of PBO@TA-APTES fibers can absorb the energy of the ultraviolet lights, thus reducing the damage of PBO fibers. This can be illustrated by the gradually decomposed TA-APTES layer and nearly undamaged PBO fibers surface as shown in Fig. 4e4–6. Compared with PBO@TA-APTES, the single fiber tensile strength and retention rate of the POSS-*g*-PBO@TA-APTES fibers increase to 3.1 GPa and 60.8%, respectively. This can be attributed to the high bond energy and excellent irradiation resistance of Si–O bonds in POSS [39]. Compared with PBO@TA-APTES, UV–vis absorption peak intensity of the POSS-*g*-PBO@TA-APTES fibers decreases significantly (Fig. 4d). Meanwhile, the introduction of POSS increases the surface roughness of PBO fibers, thus increasing the scattering of the ultraviolet lights on the surface of POSS-*g*-PBO@TA-APTES fibers and further improving its UV resistance (Fig. 4e7–9).

PBO fibers/BADCy micro-composites

Figure 5a shows the single fiber pull-out strength of PBO fibers before and after surface functionalization. The single fiber pull-out strength of POSS-*g*-PBO@TA-APTES fibers/BADCy micro-composites is increased by 31.0% to 3.8 MPa in compared with pristine PBO fibers (2.9 MPa), also higher than PBO@TA-APTES fibers/BADCy (3.6 MPa). This is because the large number of reactive groups in TA-APTES layer significantly improves the interfacial compatibility between PBO fibers and BADCy resin. Meanwhile, the introduction of TA-APTES membrane and grafting of POSS improves the surface roughness of PBO fibers, resulting in the increased mechanical engagement between PBO fibers and BADCy matrix, which is beneficial to increasing the single fiber pull-out strength of PBO fibers.

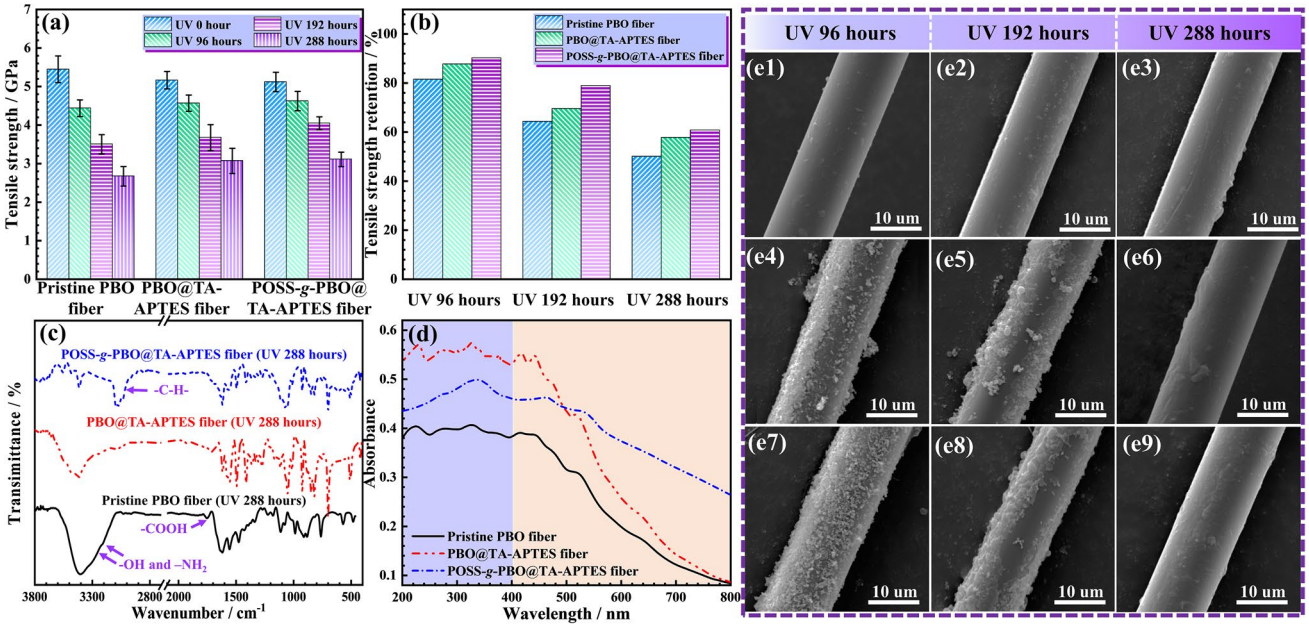

Fig. 4 Tensile strength (**a**), tensile strength retention (**b**), and FTIR spectra (**c**) of different PBO fibers after UV aging; UV–vis absorption spectra of different PBO fibers (**d**); SEM morphologies of PBO (**e1–e3**), PBO@TA-APTES (**e4–e6**), and POSS-*g*-PBO@TA-APTES (**e7–e9**) fibers surface after different UV aging time

Compared with the smooth surface of pristine PBO fibers (Fig. 5c1), obvious residual BADCy resins appear on the surface of PBO@TA-APTES fibers after single fiber pull-out test (Fig. 5c2). In addition, POSS groups on the surface of POSS-*g*-PBO@TA-APTES fibers can form physical entanglement with molecular chains of BADCy cured network [40], which further improves the single fiber pull-out strength. In Fig. 5c3, the surface of POSS-*g*-PBO@TA-APTES fibers is coarser than that of PBO@TA-APTES fibers after single fiber pull-out test. Schematic diagram of interfacial strengthening mechanism for POSS-*g*-PBO@TA-APTES fibers/BADCy micro-composites is shown in Fig. 5b.

PBO fibers/BADCy wave-transparent laminated composites

Figure 6a1–a2 show the dielectric properties of the different PBO fibers/BADCy wave-transparent laminated composites at 1 MHz and the corresponding theoretical wave-transparent performance (theoretical wave transmittance rate ($|T|^2$), reflection coefficient ($|\Gamma|^2$), and energy loss (A)). The detail formulas are shown in Supplementary Material. The POSS-*g*-PBO@TA-APTES fibers/BADCy composites display lower ε and tanδ values of 2.85 and 0.0047, respectively, than those of PBO fibers/BADCy (3.06 and 0.006) and PBO@TA-APTES fibers/BADCy (2.92 and 0.0054) at 1 MHz. In addition, it shows a higher $|T|^2$ of 93.4% than that of PBO fibers/BADCy (92.6%) and PBO@TA-APTES fibers/BADCy (93.1%). Larger interfacial polarization due to poor interfacial compatibility in the external electric field results in higher ε and tanδ values, which increases the interfacial reflection and the internal energy losses of electromagnetic wave and decreases the $|T|^2$ values. The interfacial compatibility improves as the surface activity of PBO@TA-APTES fibers is increased, thus causing the weakened charge accumulation at the interface of PBO fibers and BADCy matrix, and decreasing the ε and tanδ values. In addition, the low polar Si–O bonds and unique nanocavity of POSS further reduce the molecular polarizability and the number of polarized molecules, which further decreases the ε and tanδ of POSS-*g*-PBO@TA-APTES fibers/BADCy composites, thus increasing the $|T|^2$ values. The corresponding mechanism of improving dielectric properties for POSS-*g*-PBO@TA-APTES fibers/BADCy composites is shown in Fig. 6a3.

Based on the principle of transmission/reflection method, the electromagnetic wave transmission models of PBO fibers/BADCy composites with the different thicknesses (d, 1.5–3.5 mm) were established by the finite element analysis [41, 42]. Figure 6b–d shows the simulation results (simulated wave transmittance rate, $E_{T(simulation)}$) of wave-transparent performance at broadband (0.3–40 GHz). The detail building process of electromagnetic wave transmission models is shown in Supplementary Material. Figure 6b3–d3 are projections of the three-dimensional diagrams (Fig. 6b2–d2) of the relationship between $E_{T(simulation)}$, d, and electromagnetic wave frequency of the composites. The $E_{T(simulation)}$

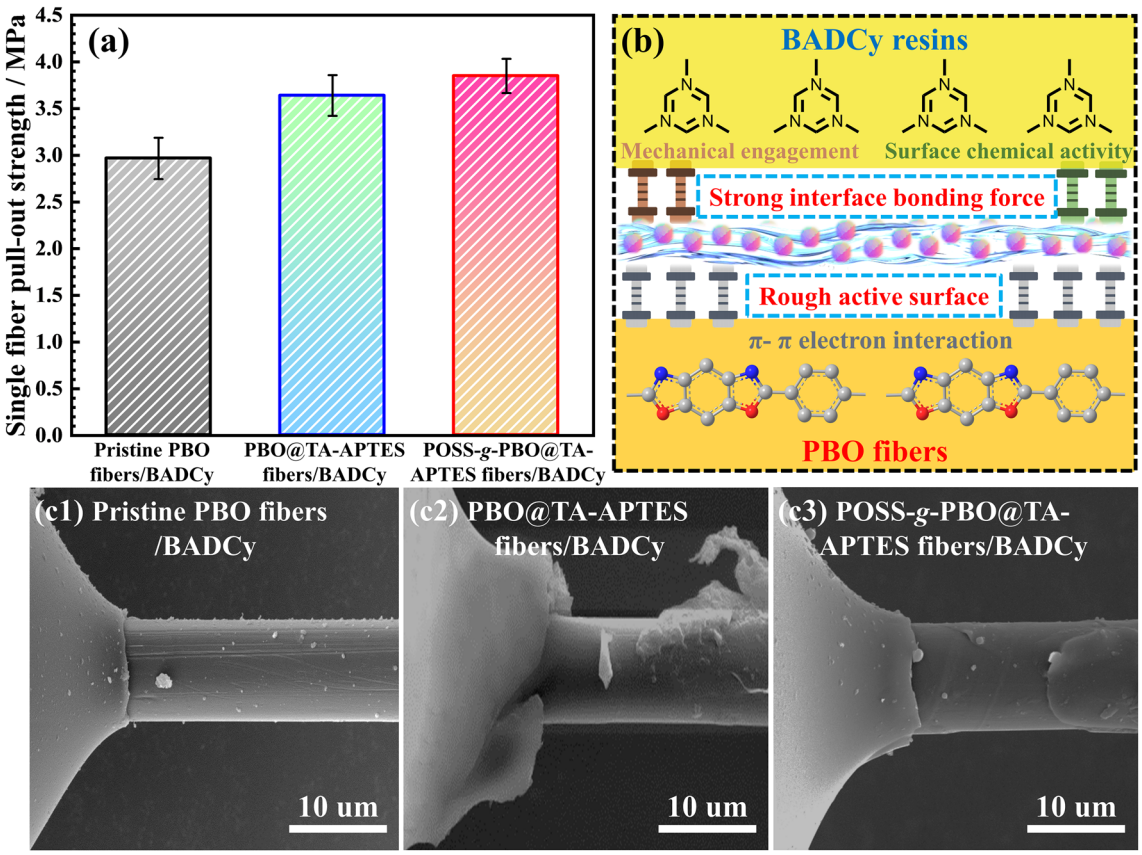

Fig. 5 Single fiber pull-out strength of PBO fibers before and after surface functionalization (**a**); Schematic diagram of interfacial enhancement mechanism of PBO fibers before and after surface functionalization (**b**); SEM images of different PBO fibers surface after single fiber pull-out test (**c1**–**c3**)

values of PBO@TA-APTES fibers/BADCy and POSS-*g*-PBO@TA-APTES fibers/BADCy composites are obviously improved in compared with PBO fibers/BADCy. The black area ($E_{T(simulation)} < 86.2\%$) gradually disappears. This is because the ε and tanδ of PBO@TA-APTES fibers/BADCy composites decrease, which weakens the interfacial reflection and the internal energy loss of the electromagnetic wave, resulting in improved $E_{T(simulation)}$ values [44]. Moreover, the low polar Si–O bonds and unique nanocavity of POSS can further decrease the ε and tan δ of POSS-*g*-PBO@TA-APTES fibers/BADCy composites, resulting in further increase of the $E_{T(simulation)}$ values.

Figure 7a demonstrates the gel contents and saturated water absorption of different PBO fibers/BADCy composites. The gel contents of PBO fibers/BADCy, PBO@TA-APTES fibers/BADCy, and POSS-*g*-PBO@TA-APTES fibers/BADCy composites are 34.1%, 35.0%, and 35.6%, respectively. The introduction of TA-APTES membrane and POSS improves the chemical inertia of PBO fibers surface, enabling PBO@TA-APTES and POSS-*g*-PBO@TA-APTES fibers to adsorb more BADCy resins [45]. The saturated water absorption of PBO fibers/BADCy, PBO@TA-APTES fibers/BADCy, and POSS-*g*-PBO@TA-APTES fibers/BADCy composites are respectively 2.5%, 2.1%, and 1.8%. This is also attributed to the significant improvement of interfacial compatibility between PBO fibers and BADCy matrix after the synergistic functionalization with TA-APTES membrane and POSS, which reduces diffusion of water, resulting the reduced final saturated water absorption. Besides, better interfacial compatibility between POSS-*g*-PBO@TA-APTES fibers and BADCy matrix leads to the higher gel contents and lower water absorption.

Figure 7b shows ILSS and flexural strength of different composites. PBO@TA-APTES fibers/BADCy composites shows improved ILSS (40.3 MPa) and flexural strength (638.6 MPa) compared to those of pristine PBO fibers/BADCy (36.7 and 587.4 MPa) while POSS-*g*-PBO@TA-APTES fibers/BADCy shows the highest ILSS and flexural strength of 42.8 and 645.8 MPa, increased by 16.6% and 9.9%, respectively. The interfacial bonding strength of PBO fibers/BADCy is highly weak, resulting the lowest ILSS (there is tiny amount of BADCy resins on the surface of PBO fibers after ILSS tests as shown

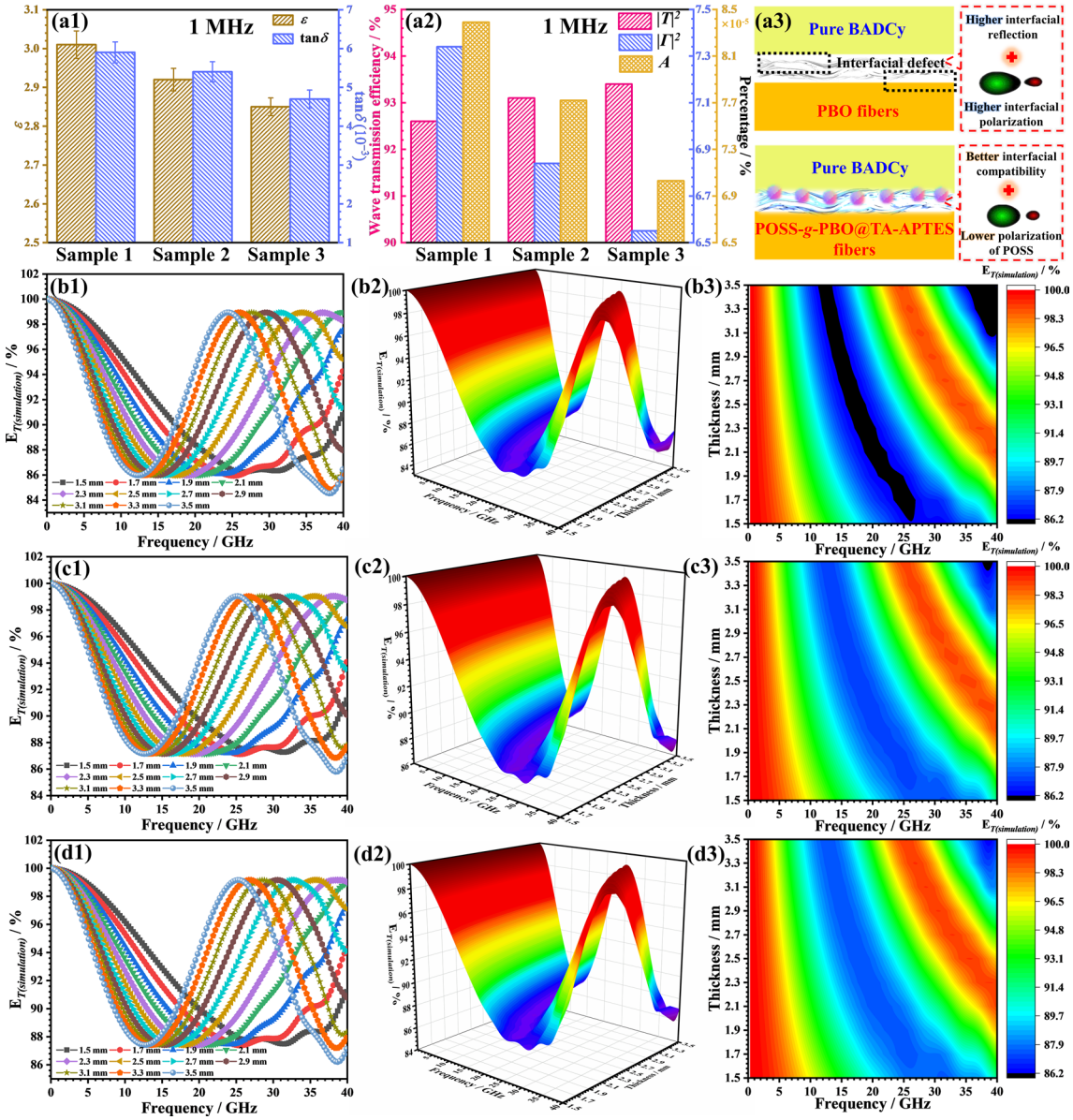

Fig. 6 Dielectric properties (**a1**–**a2**) of the PBO fibers/BADCy (Sample 1), PBO@TA-APTES fibers/BADCy (Sample 2), and POSS-*g*-PBO@TA-APTES fibers/BADCy (Sample 3) wave-transparent laminated composites at 1 MHz; Mechanism of improvement of the dielectric properties for Sample 3 (**a3**); Simulated wave-transparent performances of Sample 1 (**b1**–**b3**), Sample 2 (**c1**–**c3**), and Sample 3 (**d1**–**d3**) at 0.3~40 GHz

in Fig. S2a). The introduction of TA-APTES active layer significantly increases the surface roughness and chemical activity of PBO fibers, which effectively enhances the mechanical engagement and chemical adhesion between PBO@TA-APTES fibers and BADCy matrix (lots of BADCy resins adhere to the surface of PBO fibers and less PBO fibers detach from the BADCy matrix as shown in Fig. S2b). Furthermore, introducing POSS on the surface of POSS-*g*-PBO@TA-APTES fibers increases the surface roughness, resulting further improved mechanical properties (large number of BADCy resins adhere on the surface of POSS-*g*-PBO@TA-APTES fibers after ILSS test as shown in Fig. S2c).

Figure 7c shows the electrical insulation properties (volume resistivity (ρ_0) and breakdown strength (E_0)) of different composites. The ρ_0 and E_0 values of POSS-*g*-PBO@TA-APTES fibers/BADCy composites are respectively 2.8×10^{15} Ω·cm and 19.80 kV/mm, higher than those of PBO fibers/BADCy (2.2×10^{15} Ω·cm and 17.69 kV/mm) and PBO@TA-APTES fibers/BADCy (2.5×10^{15} Ω·cm and 18.54 kV/mm). This is due to the significantly improved interfacial compatibility

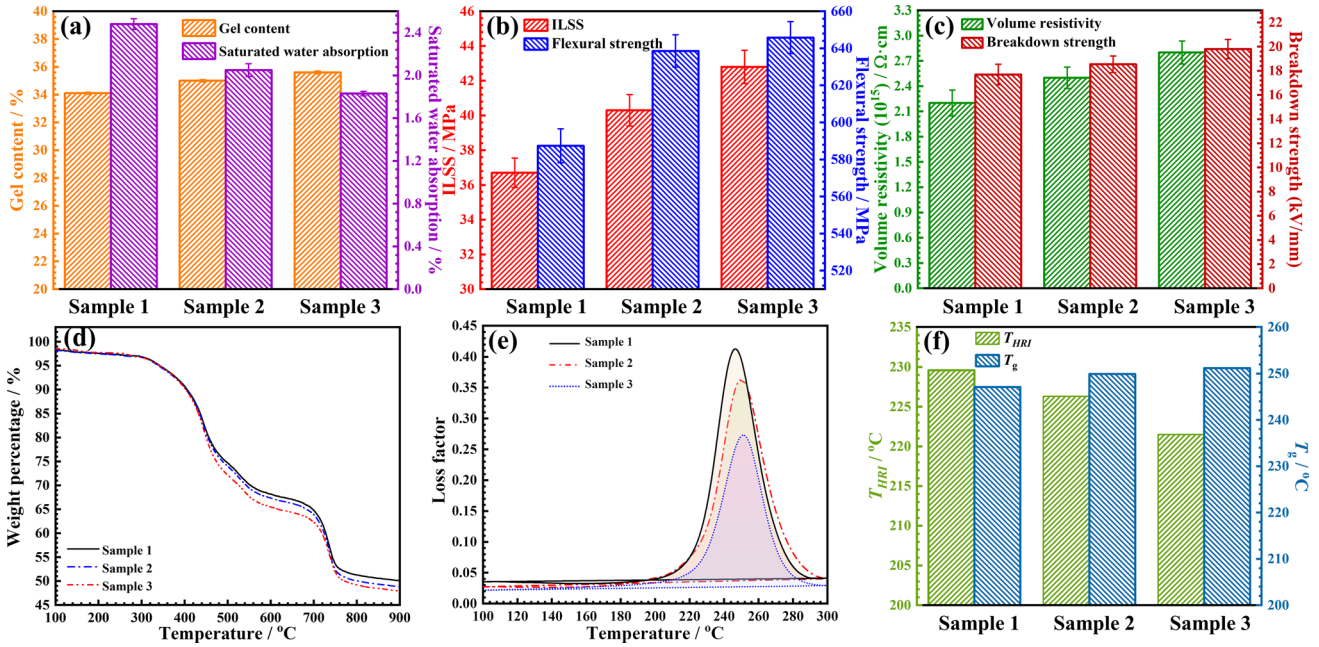

Fig. 7 Properties comparison of PBO fibers/BADCy (Sample 1), PBO@TA-APTES fibers/BADCy (Sample 2), and POSS-*g*-PBO@TA-APTES fibers/BADCy (Sample 3) wave-transparent laminated composites

between PBO@TA-APTES fibers and BADCy matrix, which reduces the defects at the interface, resulting in increased ρ_0 and E_0 values. In addition, the unique hollow structure of POSS can decrease the number of carriers and inhibit the migration of carriers, thus further increasing the ρ_0 and E_0 values of POSS-*g*-PBO@TA-APTES fibers/BADCy composites.

Figure 7d and e demonstrate the TGA and DMA curves of different composites. The corresponding $T_{Heat\text{-}resistance\ index}$ (T_{HRI}, the calculation process of T_{HRI} is shown in Table S2) and glass transition temperature (T_g) values are shown in Fig. 7f. Each of the TGA curves for three different wave-transparent laminated composites shows three weight loss stages: the volatilization of small molecules (50–300 °C), the breakage of BADCy molecular chains and carbonization (300–600 °C), and the pyrolysis of PBO fibers at higher temperature (600–900 °C). PBO@TA-APTES fibers/BADCy and POSS-*g*-PBO@TA-APTES fibers/BADCy composites show lower T_{HRI} values of 226.3 °C and 221.5 °C, respectively, than that of PBO fibers/BADCy (229.6 °C), indicating a slightly decreased thermal stability. It can be mainly ascribed to the lower thermal stability of TA-APTES and POSS hybrid membrane.

The corresponding T_g value of PBO@TA-APTES fibers/BADCy composites increases from 247.1 °C of PBO fibers/BADCy to 249.9 °C, and further increases to 251.2 °C for POSS-*g*-PBO@TA-APTES fibers/BADCy composites. This can be ascribed to the significantly promoted interfacial binding forces between PBO@TA-APTES fibers and BADCy matrix, resulting restricted rotation of molecular chains of the BADCy resins and causing an increased T_g value. Furthermore, POSS molecules can form physical entanglement points with the molecular chains of BADCy resins, thus increasing further the T_g value of POSS-*g*-PBO@TA-APTES fibers/BADCy composites. For the comparison of properties of the composites investigated in this work with those of some recent similar works, see Table S3.

Conclusions

Surface of PBO fibers is successfully functionalized by depositing the TA-APTES polymer membrane followed by the synergistic grafting of POSS (POSS-*g*-PBO@TA-APTES fibers). The interfacial interaction between PBO fibers and BADCy matrix is significantly improved by the abundant reactive groups in TA-APTES membrane. The low polar Si–O bonds and hollow structures of POSS further reduce the interfacial polarization between PBO fibers and BADCy matrix. POSS-*g*-PBO@TA-APTES fibers/BADCy composites display excellent mechanical properties, outstanding wave-transparent performance & electrical insulation properties, and excellent thermal stability. The ILSS and flexural strength of POSS-*g*-PBO@TA-APTES fibers/BADCy composites are 42.8 and 645.8 MPa, respectively, increased by 16.6% and 9.9% compared to those of PBO fibers/BADCy (36.7 and 587.4 MPa). At 1 MHz, the corresponding ε and tanδ values are reduced to 2.85 and 0.0047, respectively, lower than those of PBO fibers/BADCy (3.06 and 0.006). Meanwhile, the corresponding $E_{T(simulation)}$ of POSS-*g*-PBO@TA-APTES fibers/BADCy

composites with different thicknesses (1.5–3.5 mm) are higher than 86.2% at 0.3–40 GHz. The corresponding volume resistivity, breakdown strength, and T_{HRI} are 2.8×10^{15} Ω·cm, 19.80 kV/mm, and 221.5 °C, respectively.

Supplementary Information The online version contains supplementary material available at https://doi.org/10.1007/s42765-021-00125-4.

Acknowledgements The authors are grateful for the support and funding from National Scientific Research Project (Basis Strengthening Plan); China Postdoctoral Science Foundation (2019M653735); State Key Laboratory for Modification of Chemical Fibers and Polymer Materials from Donghua University (KF2001); State Key Laboratory of Solidification Processing in NWPU (SKLSP202103). L. Tang thanks for the Innovation Foundation for Doctor Dissertation of Northwestern Polytechnical University (CX2021036). This work is also financially supported by Polymer Electromagnetic Functional Materials Innovation Team of Shaanxi Sanqin Scholars.

Funding National Scientific Reasearch Project (Basis Strengthening Plan), China Postdoctoral Science Foundation, 2019M653735, Junliang Zhang, State Key Laboratory of Solidification Processing in NWPU, SKLSP202103, Junwei Gu, The Innovation Foundation for Doctor Dissertation of Northwestern Polytechnical University, CX2021036, Lin Tang.

Declarations

Conflict of interest There are no conflicts to declare.

References

1. Li ZF, Lu F, Lu SS, Liu H, An BY, Wang YH, Huang YD, Hu Z. Fabrication of uvioresistant poly(p-phenylene benzobisoxazole) fibers based on hydrogen bond. *J Appl Polym Sci* **2020**;*137*:48432.
2. Song B, Liu ZD, Wang TT, Wang L. Grafting of CNTs onto the surface of PBO fibers at high-density for enhancing interfacial adhesion, mechanical properties and stability of composites. *J Colloid Interf Sci* **2021**;*598*:113–25.
3. Wu SH, Li CC, Yu ZH, Ling R, Xiao YN, Zheng LC, Liu JJ, Zhang B. Nondestructive strategy to effectively enhance the interfacial adhesion of PBO/epoxy composites. *ACS Appl Mater Interfaces* **2020**;*12*:45383–93.
4. Xu JG, Hong CQ, Geng J, Jin XY, Pan YW, Wang HB, Luo XG, Zhang XH. Facile synthesis, mechanical toughening, low thermal conductivity and fire-retardant of lightweight quartz fiber reinforced polymer nanocomposites. *Compos Sci Technol* **2021**; *211*: 108836.
5. Cheng HM, Fan ZH, Hong CQ, Zhang XH. Lightweight multiscale hybrid carbon-quartz fiber fabric reinforced phenolic-silica aerogel nanocomposite for high temperature thermal protection. *Compos Part A-Appl S* **2021**; *143*: 106313.
6. Sharma V, Meena ML, Chaudhary AK, Kumar M. Cenosphere powder filled basalt fiber reinforced epoxy composite: Physical, mechanical, and thermal conductivity analysis. *Mater Today Proc* **2021**;*44*:4984–9.
7. Chen JH, Pakdel E, Xie WJ, Sun L, Xu MY, Liu QZ, Wang D. High-performance natural melanin/poly(vinyl Alcohol-co-ethylene) nanofibers/PA6 fiber for twisted and coiled fiber-based actuator. *Adv Fiber Mater* **2020**;*2*:64–73.
8. Wang L, Zhang MY, Yang B, Ding XT, Tan JJ, Song SX, Nie JY. Flexible, robust, and durable aramid fiber/CNT composite paper as a multifunctional sensor for wearable applications. *ACS Appl Mater Interfaces* **2021**;*13*:5486–97.
9. Lai XX, Guo RH, Xiao HY, Lan JW, Jiang SX, Cui C, Qin WF. Flexible conductive copper/reduced graphene oxide coated PBO fibers modified with poly(dopamine). *J Alloys Compd* **2019**;*788*:1169–76.
10. Li XT, Liu T, Jiao YZ, Dong J, Gan F, Zhao X, Zhang QH. Novel high-performance poly(benzoxazole-co-imide) resins with low dielectric constants and superior thermal stabilities derived from thermal rearrangement of ortho-hydroxy polyimide oligomers. *Chem Eng J* **2019**;*359*:641–51.
11. Liu ZD, Song B, Wang TT, Wang L. Significant improved interfacial properties of PBO fibers composites by in-situ constructing rigid dendritic polymers on fiber surface. *Appl Surf Sci* **2020**; *512*: 145719.
12. Shao Q, Lu F, Yu L, Xu XR, Huang XH, Huang YD, Hu Z. Facile immobilization of graphene nanosheets onto PBO fibers via MOF-mediated coagulation strategy: Multifunctional interface with self-healing and ultraviolet-resistance performance. *J Colloid Interf Sci* **2021**;*587*:661–71.
13. Li ZH, Yang Y, Li H, Liu LL, Zou DH. Enhancement of hydrophobicity and UV aging resistance of poly (p-phenylene benzobisoxazole) fibers modified by fluorosilane and UV absorber. *Sci Rep* **2019**;*9*:8599.
14. Jiang ZH, Tian MY, Guo ZG, Wang QC, Jia Z, Ding ZW, Jin J. Corrosion degradation behavior of PBO fibers under strong inorganic acid. *Polym Bull* **2021**;*78*:4947–58.
15. Tamargo K, Villar S, Paredes JI, Martínez A, Tascón JMD, Montes MA. Surface characterization of PBO fibers. *Macromolecules* **2003**;*36*:8662–72.
16. Liu DD, Hu J, Zhao YM, Zhou XS, Ning P, Wang Y. Surface modification of PBO fibers by argon plasma and argon plasma combined with coupling agents. *J Appl Polym Sci* **2006**;*102*:1428–35.
17. Zhang TY, Zong W, Ouyang Y, Wu Y, Miao YE, Liu TX. Carbon fiber supported binary metal sulfide catalysts with multi-dimensional structures for electrocatalytic nitrogen reduction reactions over a wide pH range. *Adv Fiber Mater* **2021**;*3*:229–38.
18. Chen L, Du Y, Huang Y, Wu F, Cheng HM, Fei B, Xin JH. Hierarchical poly(p-phenylene benzobisoxazole)/graphene oxide reinforcement with multifunctional and biomimic middle layer. *Compos Part A-Appl S* **2016**;*88*:123–30.
19. Li JW, Zhang XN, Lu YY, Linghu KL, Wang C, Ma ZL, He XH. Electrospun fluorinated polyimide/polyvinylidene fluoride composite membranes with high thermal stability for lithium ion battery separator. *Adv Fiber Mater* **2021**. https://doi.org/10.1007/s42765-021-00093-9 .
20. Liu D, Chen P, Yu Q, Ma KM, Ding ZF. Improved mechanical performance of PBO fiber-reinforced bismaleimide composite using mixed O2/Ar plasma. *Appl Surf Sci* **2014**;*305*:630–7.
21. Zhang RY, Pan XL, Jiang MW, Peng SJ, Qiu YP. Influence of atmospheric pressure plasma treatment on surface properties of PBO fiber. *Appl Surf Sci* **2012**;*261*:147–54.
22. Liu Z, Zhang JL, Tang L, Zhou YX, Lin YH, Wang RT, Kong J, Tang YS, Gu JW. Improved wave-transparent performances and enhanced mechanical properties for fluoride-containing PBO precursor modified cyanate ester resins and their PBO fibers/cyanate ester composites. *Compos Part B-Eng* **2019**; *178*: 107466.
23. Zeng J, Kong H, Du X, Xu Q, Jiang F, Li B, Yu M. Surface modification of PBO fibers with 2,2-Bis (3-amino-4-hydroxyphenyl) hexafluoropropane in supercritical carbon dioxide for enhancing interfacial strength. *Mater Today Chem* **2021**; *20*: 100426.
24. Liu RB, Han ZW, Li WF, Li XX, Zhuang QX. Improvement of the interfacial shear strength of poly(p-phenylene benzobisoxazole)

fiber/epoxy resin composite via a novel surface coating agent. *Polym Compos* **2016**;*37*:1198–205.
25. Yu L, Lu F, Huang XH, Liu YY, Li MY, Pan HZ, Wu LY, Huang YD, Hu Z. Facile interface design strategy for improving the uvioresistant and self-healing properties of poly(p-phenylene benzobisoxazole) fibers. *ACS Appl Mater Interfaces* **2019**;*11*:39292–303.
26. Chen L, Du YZ, Huang YD, Feng W, Chen HM, Xin JH. Hierarchical poly (p-phenylene benzobisoxazole)/graphene oxide reinforcement with multifunctional and biomimic middle layer. *Compos Part A-Appl S* **2016**;*88*:123–30.
27. Shao Q, Hu Z, Xu XR, Yu L, Zhang DY, Huang YD. Mussel-inspired immobilization of BN nanosheets onto poly(p-phenylene benzobisoxazole) fibers: Multifunctional interface for photothermal self-healing. *Appl Surf Sci* **2018**;*440*:1159–65.
28. Tang YS, Dong WC, Tang L, Zhang YK, Kong J, Gu JW. Fabrication and investigations on the polydopamine/KH-560 functionalized PBO fibers/cyanate ester wave-transparent composites. *Compos Commun* **2018**;*8*:36–41.
29. Wang ZX, Ji SQ, Zhang J, He F, Xu ZD, Peng SQ, Li YX. Dual functional membrane with multiple hierarchical structures (MHS) for simultaneous and high-efficiency removal of dye and nano-sized oil droplets in water under high flux. *J Membrane Sci* **2018**;*564*:317–27.
30. Wang ZX, Ji SQ, Zhang J, Liu QX, He F, Peng SQ, Li YX. Tannic acid encountering ovalbumin: a green and mild strategy for superhydrophilic and underwater superoleophobic modification of various hydrophobic membranes for oil/water separation. *J Mater Chem A* **2018**;*6*:13959–67.
31. Wang ZX, Yang HC, He F, Peng SQ, Li YX, Shao L, Darling SB. Mussel-inspired surface engineering for water-remediation materials. *Mat* **2019**;*1*:115–55.
32. Wang ZX, Han MC, Zhang J, He F, Xu ZD, Ji SQ, Peng SQ, Li YX. Designing preferable functional materials based on the secondary reactions of the hierarchical tannic acid (TA)-aminopropyltriethoxysilane (APTES) coating. *Chem Eng J* **2019**;*360*:299–312.
33. Wang ZX, Ji SQ, He F, Cao MY, Peng SQ, Li YX. One-step transformation of highly hydrophobic membranes into superhydrophilic and underwater superoleophobic ones for high-efficiency separation of oil-in-water emulsions. *J Mater Chem A* **2018**;*6*:3391–6.
34. Li SM, Zhu YF, Wang Y, Wang BR, Huang YD, Yu T. Cyanate ester resin based composites with high toughness and low outgassing performances. *Compos Commun* **2021**; *23*:100574.
35. Zhou ZX, Li YW, Zhong J, Luo Z, Gong CR, Zheng YQ, Peng SQ, Yu LM, Wu LX, Xu Y. High-performance cyanate ester resins with interpenetration networks for 3D printing. *ACS Appl Mater Interfaces* **2020**;*12*:38682–9.
36. Huang S, Wang L, Li YC, Liang CB, Zhang JL. Novel $Ti_3C_2T_x$ MXene/epoxy intumescent fire-retardant coatings for ancient wooden architectures. J Appl Polym Sci **2021**;*138*:e50649.
37. Gu JW, Li Y, Liang CB, Tang YS, Tang L, Zhang YK, Kong J, Liu H, Guo ZH. Synchronously improved dielectric and mechanical properties of wave-transparent laminated composites combined with outstanding thermal stability by incorporating iysozyme/POSS functionalized PBO fibers. *J Mater Chem C* **2018**;*6*:7652–60.
38. Taloub N, Henniche A, Liu L, Li J, Rahoui N, Hegazy M, Huang YD. Improving the mechanical properties, UV and hydrothermal aging resistance of PIPD fiber using MXene (Ti3C2(OH)2) nanosheets. *Compos Part B-Eng* **2019**;*163*:260–71.
39. Qiao XX, Zhou Z, Zhang JC, Mo J, Chen GX, Li QF. Synthesis, characterization, and properties of novel UV-resistant poly (urethane-imide)/POSS nanocomposite. *High Perform Polym* **2018**;*30*:1210–8.
40. Ma LC, Zhu YY, Wang MZ, Yang XB, Song GJ, Huang YD. Enhancing interfacial strength of epoxy resin composites via evolving hyperbranched amino-terminated POSS on carbon fiber surface. *Compos Sci Technol* **2019**;*170*:148–56.
41. Liu Z, Zhang JL, Tang YS, Xu JB, Ma H, Kong J, Gu JW. Optimization of PBO fibers/cyanate ester wave-transparent laminated composites via incorporation of a fluoride-containing linear interfacial compatibilizer. *Compos Sci Technol* **2021**; *210*: 108838.
42. Liu Z, Fan XL, Zhang JL, Yang ZY, Tang YS, Li JW, Kong J, Gu JW. Improving the comprehensive properties of PBO fibres/cyanate ester composites using a hyperbranched fluorine and epoxy containing PBO precursor. *Compos Part A-Appl S* **2021**; *150*: 106596.
43. Qin M, Zhang L, Zhao X, Wu HJ. Lightweight Ni foam-based ultra-broadband electromagnetic wave absorber. *Adv Funct Mater* **2021**;*31*:2103436.
44. Xia L, Yang YN, Zhang XY, Zhang J, Zhong B, Zhang T, Wang HT, Wen GW. Crystal structure and wave-transparent properties of lithium aluminum silicate glass-ceramics. *Ceram Int* **2018**;*44*:14896–900.
45. Tang L, Yang ZY, Tang YS, Zhang JL, Kong J, Gu JW. Facile functionalization strategy of PBO fibres for synchronous improving the mechanical and wave-transparent properties of the PBO fibres/cyanate ester laminated composites. *Compos Part A- Appl S* **2021**; *150*:106622.

Zheng Liu is currently a PhD candidate in Chemistry at Northwestern Polytechnical University. He received the bachelor's degree and master's degree from Nanchang Hangkong University in 2018 and Northwestern Polytechnical University in 2021, respectively. His research is focused on the fiber reinforced polymer matrix wave-transparent composites.

Xiaoli Fan received her PhD degree from the Chinese University of Hong Kong in 2005. Currently she is a full professor of School of Materials Science and Engineering at Northwestern Polytechnical University. His main research interests include two-dimensional magnetic materials and catalytic materials for electrochemical reaction.

Lei Cheng received his Master's degree from the Northwestern Polytechnical University in 2010. Currently he is a senior engineer at Aerospace Research Institute of Materials and Processing Technology. His research is focused on the carbon fiber reinforced polymer matrix composites.

Junliang Zhang received his PhD degree from the University of Warwick, UK, in 2017. After the postdoctoral fellowship at the Friedrich Schiller University Jena in Germany, he joined the School of Science at Northwestern Polytechnical University in 2018. His main research interests include intrinsic thermal conductivity polymers and fiber reinforced polymer matrix wave-transparent composites.

Lin Tang is currently a PhD candidate in Materials Science at Northwestern Polytechnical University. He received the bachelor's degree from Northwestern Polytechnical University in 2018. His research is focused on the fiber-reinforced polymer matrix wave-transparent composites.

Yusheng Tang received his PhD degree from Northwestern Polytechnical University in 2007. Currently he is a full professor of School of Chemistry and Chemical Engineering at Northwestern Polytechnical University. His research interests include fiber-reinforced polymer matrix wave-transparent composites, and electromagnetic wave absorbing materials.

Jie Kong received his PhD degree from Northwestern Polytechnical University in 2004. He then went to The Hong Kong Polytechnic University as a postdoctoral fellow and the University of Bayreuth as an Alexander von Humboldt research fellow. In 2011, he joined the School of Science at Northwestern Polytechnical University as a full professor. His research interests include hyperbranched polymers, ceramic precursors and electromagnetic wave absorbing/transmitting materials.

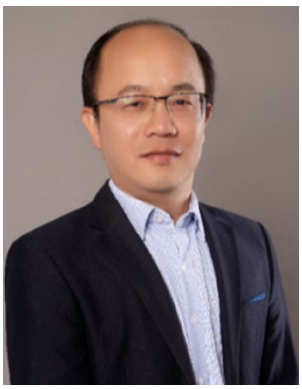

Junwei Gu received his PhD degree from Northwestern Polytechnical University in 2010. Currently he is a full professor of School of Chemistry and Chemical Engineering at Northwestern Polytechnical University. His research interests include thermally conductive polymers and composites, fiber reinforced polymer matrix wave-transparent composites, and electromagnetic interference shielding polymer matrix composites.